APL Materials

RESEARCH ARTICLE | APRIL 18 2025

β-Ga_2O_3:Cr nanowires with optical microcavities for determining local heating induced by x-ray nanobeams

Special Collection: Ultrawide Bandgap Semiconductors

D. Carrasco; J. Dolado ; P. Pérez-Peinado; B. Rodríguez; M. Alonso-Orts ; J. M. San Juan; M. L. Nó; P. Hidalgo; G. Martínez-Criado ; B. Méndez ; E. Nogales

APL Mater. 13, 041115 (2025)
https://doi.org/10.1063/5.0261501

AIP Publishing

β-Ga_2O_3:Cr nanowires with optical microcavities for determining local heating induced by x-ray nanobeams

Cite as: APL Mater. 13, 041115 (2025); doi: 10.1063/5.0261501
Submitted: 30 January 2025 • Accepted: 1 April 2025 •
Published Online: 18 April 2025

D. Carrasco,[1] J. Dolado,[2] P. Pérez-Peinado,[1] B. Rodríguez,[1] M. Alonso-Orts,[3] J. M. San Juan,[4] M. L. Nó,[4] P. Hidalgo,[1] G. Martínez-Criado,[2,5] B. Méndez,[1] and E. Nogales[1,a)]

AFFILIATIONS

[1] Departamento de Física de Materiales, Facultad de Ciencias Físicas, Universidad Complutense de Madrid, 28040 Madrid, Spain
[2] European Synchrotron Radiation Facility, 38043 Grenoble, France
[3] Institute of Solid State Physics, University of Bremen, Otto-Hahn-Allee 1, 28359 Bremen, Germany
[4] Departamento de Física, Facultad de Ciencia y Tecnología, Universidad del País Vasco UPV/EHU, Apdo. 644, 48080 Bilbao, Spain
[5] Instituto de Ciencia de Materiales de Madrid, CSIC, 28049 Madrid, Spain

Note: This paper is part of the Special Topic on Ultrawide Bandgap Semiconductors.
[a)] **Author to whom correspondence should be addressed:** enogales@ucm.es

ABSTRACT

This study explores the x-ray excited optical luminescence (XEOL) of optical microcavities fabricated in β-Ga_2O_3:Cr nanowires (NWs). XEOL measurements reveal prominent luminescence bands in the near ultraviolet-blue (NUV-B) and in the red-near infrared (R-NIR) spectral regions. The NUV-B emission originates from β-Ga_2O_3 defects, while the R-NIR band is attributed to Cr^{3+} intraionic transitions. Both spectral regions exhibit sharp resonances, which are analyzed as Fabry–Pérot and whispering gallery mode resonances. Exposure to x-ray nanobeam induces a redshift of the sharp R-NIR peaks, attributed to local temperature increase in the NWs caused by x-ray absorption. The influence of this temperature rise on the NUV-B peaks is also evaluated. In addition, the local temperature increase due to x-ray absorption is estimated through COMSOL finite-difference time-domain simulations, incorporating the material's physical and thermal properties. This work demonstrates the application of β-Ga_2O_3:Cr optical microcavities as luminescence-based nanothermometers to probe the localized effects of x-ray nanobeam irradiation.

INTRODUCTION

Since Higashiwaki *et al.*[1] demonstrated a field-effect transistor based on the ultra-wide bandgap semiconductor monoclinic gallium oxide (β-Ga_2O_3) and highlighted its exceptionally high breakdown field, considerable effort has been directed toward developing high-power electronics utilizing this material. β-Ga_2O_3's electronic properties overcome some limitations of commonly used high-power electronic materials, such as silicon carbide (SiC) and gallium nitride (GaN). In addition, β-Ga_2O_3 is known for its robust chemical and thermal stability, as well as its strong resistance to radiation.[2] However, it also presents notable challenges for electronic device applications, particularly its low thermal conductivity.[3] Thus, quantitatively assessing local heating in high power electronic and photonic devices based on β-Ga_2O_3 is essential.

Thermometers designed for local thermal assessment in these devices, especially in demanding fields such as aeronautics and deep-space environments, must be capable of measuring a broad temperature range, maintain stability under extreme conditions, and feature minimal spatial dimensions.[3] Remote temperature sensing

using optical transducing mechanisms, such as luminescence nanothermometry, provides a highly accurate approach for thermal measurements.[4]

Several thermometers based on β-Ga_2O_3 have been reported, including some utilizing nanostructures[5] and others employing optical spectroscopy of Cr-doped bulk samples.[6] Recently, we demonstrated two different architectures for micro-thermometers based on photoluminescence (PL) spectroscopy within optical microcavities created from Cr-doped β-Ga_2O_3 micro- and nanowires. In one of them, we fabricated optical cavities along β-Ga_2O_3 nanowires (NWs) by defining pairs of distributed Bragg reflectors (DBRs) through focused ion beam (FIB) milling.[7] This approach presents several advantages, enabling high contrast DBRs that function as tunable mirrors. These can be employed across the red-near-infrared (R-NIR) range in Cr-doped NWs[7] as well as in the near-ultraviolet-blue (NUV-B) range in unintentionally doped NWs.[8]

In the second approach, the microwires were encapsulated into DBRs made by alternating Al_2O_3/TiO_2 layers.[9] These approaches allowed for temperature measurements across a broad range—at least from 100 to 550 K—by tracking spectral shifts of two distinct luminescence features: the Cr^{3+} R lines and the optical cavity Fabry–Pérot (FP) resonances.[9–11] In addition, other types of sensors have been demonstrated in this material, such as pressure sensors based on Ga_2O_3:Cr, as developed by Barmore *et al.*[12]

Fourth-generation synchrotron x-ray sources, such as the Extremely Brilliant Source upgrade at the European Synchrotron Radiation Facility (ESRF-EBS), offer unprecedented levels of flux and coherence, enabling nanoscale resolution for a wide range of techniques. However, these enhanced capabilities also introduce increasing risks of radiation-induced damage. Addressing experimentally the beam-induced heating, a critical aspect of radiation effects by directly quantifying the local temperature increase induced by the x-ray nanobeam would be of great interest.[13,14] Sample heating can cause both permanent damage (e.g., structural changes, oxidation) and non-destructive alterations that compromise measurement accuracy, such as thermal expansion, sample drift, increased chemical reactivity, or changes in electrical conductivity. Most previous studies on beam heating are based on simulations, and direct experimental validation of these models remains limited.

In this study, we employ the previously developed thermometer[10] to investigate thermal heating in Cr-doped β-Ga_2O_3 NWs using the nano-analysis ID16B beamline at the European Synchrotron Radiation Facility (ESRF).[15] By leveraging the beamline's high spatial resolution (achieving a beam diameter below 100 nm) and the capabilities of x-ray excited optical luminescence (XEOL) spectroscopy, we estimate the local temperature within the NW microcavities by monitoring luminescence spectral shifts. In addition, XEOL analysis reveals resonances in the NUV-B spectral range, whose underlying physical mechanisms are thoroughly examined.

EXPERIMENTAL

The Cr-doped β-Ga_2O_3 NWs were synthesized using a thermal evaporation method, as detailed in Ref. 7. Optical cavities were created by milling two DBRs using a FEI Helios NanoLab 650 focused ion beam (FIB) system.[7] Commercial *OptiFDTD* photonic simulation software has been used to design the DBRs for the optical cavities, determine the resonances, and map the confined modes in the cavities.

The morphology of the samples was examined with a Thermo Fisher-Prisma scanning electron microscope (SEM). X-ray excited optical luminescence (XEOL) measurements were carried out at the nano-analysis beamline ID16B of the ESRF.[15] A monochromatic x-ray beam with an energy of 10.52 keV, focused to a spot of 80 nm diameter, was used at varying intensities ranging from 10^9 to 10^{11} photons per second. Another operation mode has also been used, the pink mode, where the beam had similar dimensions but a different photon energy, namely 17.5 keV. In this case, the photon flux ranged from 1.1×10^{10} to 1.1×10^{11} photons per second. COMSOL Multiphysics software has been used to simulate the eventual heating of the wire caused by the x-ray beam. The optical signals were detected in backscattering geometry, where a far-field optical collection system was employed. The collected light was then transmitted through an optical fiber to a spectrometer for spectral analysis. The spectrometer was equipped with a Si CCD detector, allowing precise fast acquisition of the emitted luminescence in a single shot. All spectra were acquired at nominal room temperature.

RESULTS AND DISCUSSION

Figure 1(a) shows an SEM image of the optical microcavities created along the NW. The structure consists of four DBRs, which define three optical cavities—labeled C1, C2, and C3—where light is confined. The crystal orientation was previously characterized with polarized Raman spectroscopy,[10] revealing that the wire axis aligns with the [001] crystal direction, while the upper surface corresponds to the (100) crystal plane. Figure 1(b) presents a schematic of the geometry used to measure the spatially resolved XEOL signal from the cavity. Both the unconfined luminescence, emitted directly from the point excited by the x-ray beam, and the confined light, scattered at the edge of each DBR, are measured.

Figure 1(c) presents a map of the XEOL signal across the entire spectral range, acquired from the region outlined by the red rectangle in Fig. 1(a). This map includes the optical cavity C1, defined by the two central DBRs, as well as portions of the adjacent, lateral optical cavities C2 and C3. The x-ray flux for all the XEOL measurements shown in Fig. 1 was 2.6×10^{10} photons per second, and the photon energy is 10.52 keV. The red regions in Fig. 1(c) represent the highest emitted intensity, while the dark blue regions indicate the lowest intensity. Figure 1(d) displays the spectra obtained from the points labeled in Fig. 1(c). The local XEOL spectra vary from one point to another. The XEOL emission primarily occurs in the NUV-B and R-NIR spectral ranges, resembling previously reported PL and cathodoluminescence (CL) spectra for Cr-doped β-Ga_2O_3.[6,16] The NUV-B band is a characteristic complex band, attributed to intrinsic defects or self-trapped holes.[17] Figure 1(e) shows the XEOL spectrum obtained from point 3 in Fig. 1(c), polarized along the NW axis (corresponding to the *c*-crystal direction[10]), leveraging the linear polarization of the x-ray nanobeam. The sharp NUV-B peaks appear at identical wavelength positions to those observed in the unpolarized spectrum presented in Fig. 1(d).

Resonance peaks in the R-NIR region are significantly amplified compared to the broader NUV-B and R-NIR bands when

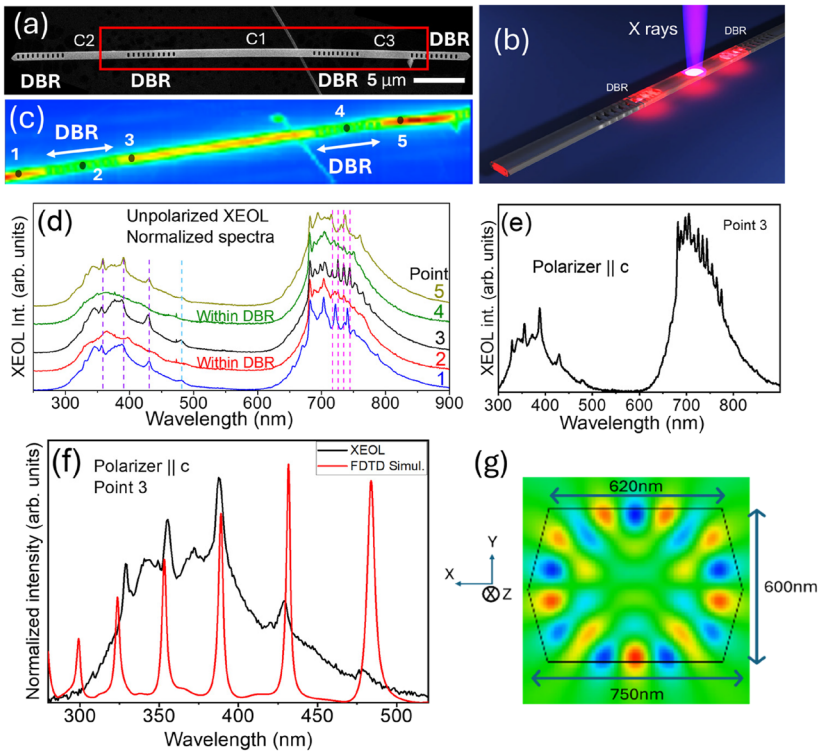

FIG. 1. (a) SEM image showing the optical cavity created in the NW by forming two DBRs using a FIB. (b) Schematic illustration of the experimental measurement. (c) XEOL intensity map of the region marked with a red rectangle in (a). (d) Local XEOL spectra obtained from the points labeled with numbers in (c). The optical cavity is located between the two DBRs, with point 3 situated inside this cavity. (e) Polarized XEOL spectrum measured at point 3. (f) Comparison of XEOL spectrum polarized along c-direction with FDTD simulations showing WGM peaks for the cavity. The x-ray flux used in the XEOL measurements was 2.6×10^{10} photons per second. (g) Cross-sectional view from the FDTD simulation showing the E_z component of the electromagnetic field within the wire.

exciting points 1, 3, and 5 [see Figs. 1(c) and 1(d)]. These peaks in the R-NIR band are attributed to longitudinal FP resonances within the optical cavity C1 (L = 13 μm), as previously discussed. Interestingly, several resonance peaks are also observed in the NUV-B band. These peaks, at 356, 387, 428, and 479 nm, exhibit a free spectral range (FSR)—the separation between consecutive peaks—that is too large to be explained by longitudinal FP modes. For example, the FSR for the peak at 428 nm should follow the formula $\Delta\lambda_{FSR} = \lambda^2/(2Ln_g)$, where n_g is the group refractive index of the material, λ is the position of the reference resonance peak, and L is the cavity length. Using $n_g = 2.1$ at $\lambda = 430$ nm nm[18] and cavity length $L = 13$ μm, as determined from the SEM image in Fig. 1(a), the calculated FSR value would be $\Delta\lambda_{FSR,calc} = 3.2$ nm. This is an order of magnitude smaller than the experimentally observed $\Delta\lambda_{FSR,exp} = 428–387 = 41$ nm. Thus, the longitudinal FP resonances between the two DBRs defining the C1 cavity are excluded as the origin of the NUV-B peaks.

Transversal FP modes, oriented parallel to the vertical direction [i.e., perpendicular to the plane in Fig. 1(a)], were also ruled out because the cavity dimensions (a thickness of ~600 nm, as measured by SEM[19]) do not match the observed FSR. Moreover, the reflectivity at the material–air interface—due to the refractive index contrast—is insufficient to account for the relatively high finesse values seen experimentally.

Another possible explanation for these peaks is the whispering gallery modes (WGMs), where optical paths are confined within a smaller region, resulting in a larger FSR. Due to the total internal reflection of light within the material, WGMs exhibit higher reflectivity, which translates into higher finesse values. To investigate the origin of these NUV-B peaks, finite-difference time-domain (FDTD) simulations were performed using the OptiFDTD software.[7] Figure 1(f) presents the simulated spectrum, superimposed and normalized to the XEOL spectrum within the specified wavelength range. The simulation is based on the cross-sectional dimensions of the NW, as determined by SEM and illustrated in Fig. 1(g). The simulated sharp peaks are closely aligned with the experimentally observed peaks in the XEOL spectrum. Figure 1(g) depicts the cross-sectional standing wave pattern of the E_z component of the electromagnetic field inside the wire. The pattern, characterized by maxima (red) and minima (blue), confirms the presence of WGMs, thereby identifying them as the origin of the NUV-B resonances.

Figure 2 illustrates the significant impact of the x-ray beam power on the local XEOL spectra from the microcavity. X-ray beam operated in the 7/8 + 1 filling mode (10.52 keV) or the pink mode (17.5 keV). First, the intensity ratio between the NUV-B and R-NIR bands changes drastically as the photon flux (beam power) varies from 10^9 photons per second (1.7 μW) to 4.6×10^{11} photons per second (775.2 μW), as shown in Fig. 2(a) (7/8 + 1 filling mode). At the lower excitation density, the NUV-B band is effectively quenched. The decay times of the two bands differ by several orders of magnitude. The main contribution to the NUV-blue band has a lifetime in the range of 10^{-8} seconds, with a component in the range of milliseconds several orders of magnitude weaker.[20] On the other hand, the R-NIR lifetime, at room temperature, exhibits a lifetime in the range of 10^{-4} s.[16] The R-NIR band originates from Cr^{3+} intraionic transitions[7,10,16,21] and includes two sharp R-lines (corresponding to the ^2E–$^4A_2$ transition) and a broader, phonon-assisted band

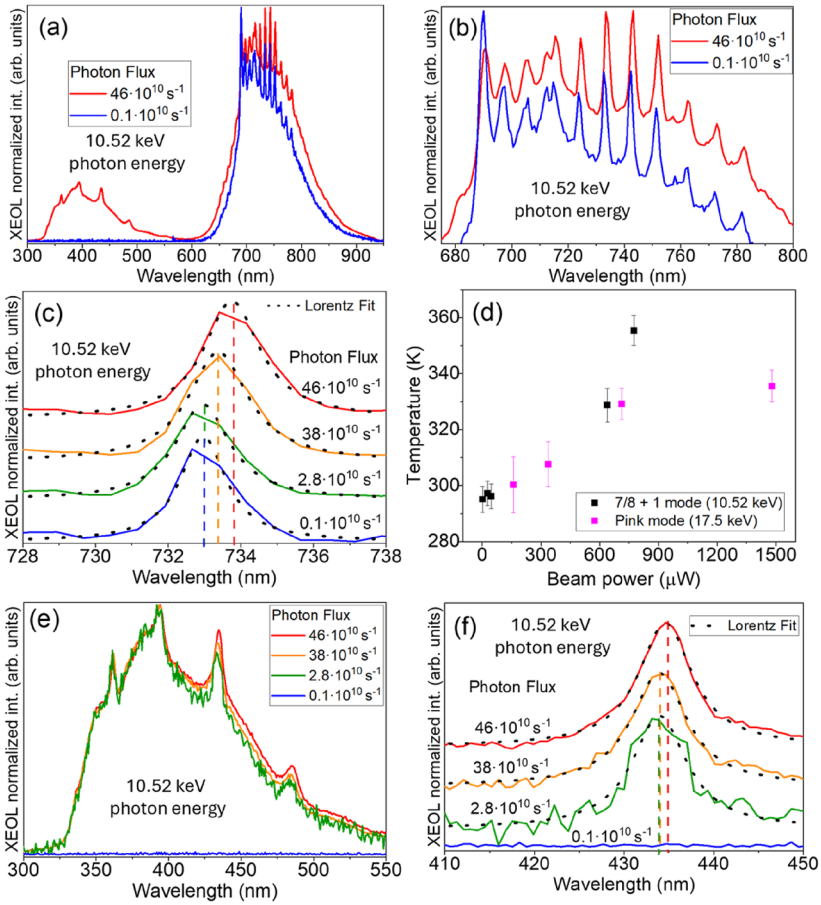

FIG. 2. (a) XEOL spectra for different photon fluxes and a photon energy of 10.52 keV (above the Ga K-edge), showing both the characteristic NUV-B and R-NIR luminescence bands of β-Ga_2O_3:Cr. (b) Magnified view of the R-NIR FP resonances from (a), highlighting shifts in the R-lines and FP peaks, along with variations in the relative intensities of the R-lines, driven by x-ray-induced local heating within the cavity. (c) Lorentzian fits to a selected resonance under various photon fluxes, revealing a clear wavelength shift. (d) Local temperature of the cavity vs photon flux. (e) NUV-B resonances measured under varying x-ray beam fluxes. (f) Close-up view of one of the peaks shown in (e), with the dashed vertical lines marking the observed spectral shift.

(resulting from the $^4T_2$–$^4A_2$ transition). At relatively low excitation densities, the R-NIR band dominates the luminescence entirely. However, as the excitation density significantly increases, the slower red-NIR luminescence saturates, leading to a strong enhancement of the NUV-blue band.

Focusing on the R-NIR band, we observe a pronounced redshift of the FP interference peaks as the excitation density increases, as shown in Fig. 2(b). In addition, the relative intensity of the R-lines decreases compared to the broader band, consistent with the expected behavior at elevated temperatures.[16,21] These findings provide clear evidence of a significant rise in local temperature with increasing x-ray excitation density.

Figure 2(c) highlights the detailed wavelength shift of the peak centered around 733 nm for a photon energy of 10.52 keV and various excitation photon fluxes, with the flux values indicated for each spectrum. For fluxes (powers) below 2×10^{10} photons per second (34 μW), the shift is nearly imperceptible within the experimental uncertainty. Applying the calibration curve for this thermometer,[10] the local temperature of the cavity was obtained as a function of the beam power for the two filling modes, as shown in Fig. 2(d). The thermal resolution ranges from 0.3 to 0.9 K, and the thermal sensitivity ranges from 1.3% K^{-1} to 2.1% K^{-1} in the probed temperature range (150–400 K).

In the NUV-B band [Fig. 2(e)], several peaks are observed and attributed to WGMs, as previously discussed. In this system, these peaks have a larger full-width at half-maximum (FWHM) compared to the FP resonances in the R-NIR region [see Fig. 2(c)]. Similar to the R-NIR peaks, the NUV-B peaks display a temperature-dependent redshift. However, due to quenching of the NUV-B band at lower photon fluxes, its spectral shift cannot be determined in this range. Nonetheless, the analysis of the R-NIR peaks suggests that irradiation at lower fluxes does not induce significant heating in the NW.

To estimate the expected heating caused by the x-ray nanobeam in the optical cavity, we applied the model described by Bonino *et al.*[14] The classical Fourier heat diffusion equation was used to describe the temperature distribution,

$$\rho C_p \frac{\partial T}{\partial t} + \nabla \cdot (-k_T \nabla T) = Q, \tag{1}$$

where $T = T(x,y,z,t)$ is the temperature, ρ is the density of the medium, C_p is its heat capacity at constant pressure, and k_T is the thermal conductivity. The boundary conditions assumed that the NW is surrounded by air at a constant temperature of 295.2 K along

all boundaries. The heat source for a NW irradiated by the x-ray nanobeam was modeled by[14]

$$Q_{im}(x,y,z,t) = \frac{2\phi(t)E_0}{\pi W_x W_z \lambda} \exp\left[-\left(\frac{y}{\lambda} + \frac{2x^2}{W_x^2} + \frac{2z^2}{W_z^2}\right)\right], \quad (2)$$

where $\phi(t)$represents the instantaneous photon flux, λ is the energy dependent material's attenuation length as obtained by PyMca software,[22] E_0 is the energy of the x-ray photons, and W_x and W_z are defined as

$$W_i = \frac{FWHM_i}{\sqrt{2\ln 2}} \simeq 0.85 FWHM_i; \quad i = x, z.$$

Simulations were carried out with the photon energies of the two operation modes, i.e., $E_{0,7/8+1}$ = 10.52 keV (7/8 + 1 mode) or $E_{0,pink}$ = 17.5 keV (pink mode). Although the beam is pulsed, the spectral shift of the FP peaks is averaged, resulting in a stationary thermal regime. The total time-averaged power density absorbed by the NW was obtained by substituting the instantaneous photon flux $\phi(t)$ with the experimental time-averaged photon flux $\overline{\Phi}_0$, which ranges from 10^9 photons per second to 4.6×10^{11} photons per second in the 7/8 + 1 mode, as shown in Fig. 2. In the case of the pink mode, the flux ranges from 1.1×10^{10} photons per second to 1.1×10^{11} photons per second.

In the stationary regime, given that k_T is anisotropic in β-Ga_2O_3, Eqs. (1) and (2) combine into

$$\begin{aligned} &\rho C_p \frac{\partial T}{\partial t} + \nabla \cdot (-k \nabla T) = Q(x,y,z) \\ &\Rightarrow \quad \rho C_p \frac{\partial T}{\partial t} + \sum_{x_i = x,y,z} \frac{\partial}{\partial x_i}\left(k_T \frac{\partial T}{\partial x_i}\right) \\ &= -\frac{2\overline{\Phi}_0 E_0}{\pi W_x W_z \lambda} \exp\left[-\left(\frac{y}{\lambda} + \frac{2x^2}{W_x^2} + \frac{2z^2}{W_z^2}\right)\right]. \end{aligned} \quad (3)$$

To compare the experimental results with the predicted values from the x-ray absorption models, COMSOL FDTD simulations were performed to solve Eq. (3). The temperature distribution was calculated along the optical cavity for several photon fluxes at each operation mode. The NW model, surrounded by air, had dimensions a = 620 nm, b = 730 nm, L = 13 μm, and DBR hole sizes α = 185 nm, β = 290 nm, and γ = 385 nm, as determined by SEM measurements.

The temperature-dependent experimental parameters used in the simulation of Eq. (3), along with references to the corresponding sources, are listed in Table I. The results, shown in Fig. 3(a), predict a perfectly linear dependence at each operation mode and a clearly different slope due to the fact that attenuation coefficient is larger for 10.52 keV than for 17.5 keV photon energy in Ga_2O_3. To compare these simulations with the experimental data inferred from the

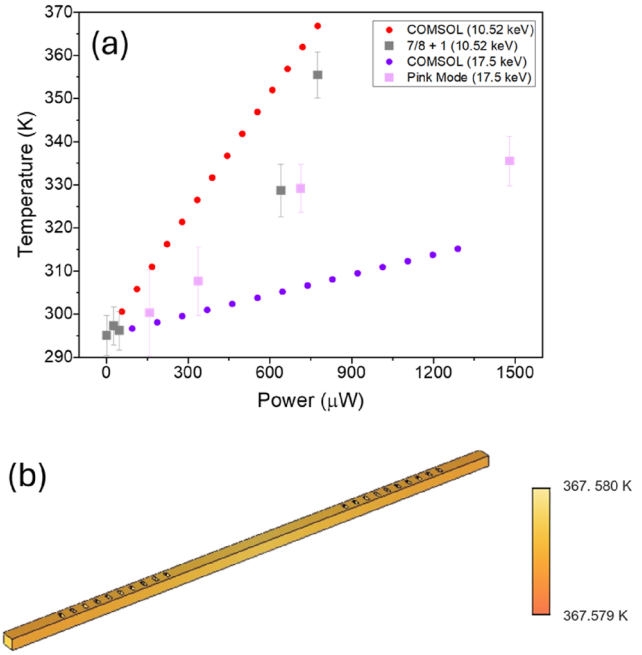

FIG. 3. (a) Temperature variation of the cavity for different beam powers in the two different beam filling modes as calculated by COMSOL. (b) Model used for the COMSOL simulations to obtain the temperature distribution along the NW axis when irradiated by the x-ray beam at its center with 10.52 keV and the highest photon flux. The resulting temperature distribution remains nearly constant along the wire.

FP peak positions of the microthermometer [see Fig. 2(d)], the latter has also been included in light colors in Fig. 3(a). They suggest a trend that may deviate slightly from linearity, particularly at higher energies. The simulations, while valuable, carry uncertainties, e.g., in material parameters or boundary conditions that are difficult to quantify and should be considered as approximate. Further investigation will be needed to fully understand the nature of the power dependence.

A question that is raised is if there is an appreciable temperature variation from the small area irradiated with the x-ray beam—a circle with an 80 nm diameter—to the region defined by the DBRs, which are 6.5 μm away from the center of the cavity. If there was a significative temperature gradient, the value deduced from the FP peak shift would be an average of the temperatures present along the optical cavity. To clarify this point, the simulations of the temperature distribution along the wire after a few seconds of irradiation,

TABLE I. Parameters for Eq. (3).

E_0 (keV)	$k_{T,z}$ (W/m K) Ref. 23	C_p (J/kg K) Ref. 23	*Density* (kg/m^3) Ref. 24	α (m^{-1}) Ref. [PyMca]
10.52 17.5	8140 * T$^{-1.12}$	186.55–32514 T$^{-1.1647}$	5974–0.08 T	40 000 10 800

which is the time required to obtain the XEOL spectra shown in Figs. 1 and 2, were analyzed. Figure 3(b) shows these results, where a minimal variation along the length of the cavity is obtained. In particular, the temperature difference between the cavity center and its extremities is only 3×10^{-5} K for the highest flux and 1×10^{-7} K for the lowest flux. Consequently, this temperature variation is several orders of magnitude below the experimental uncertainty, allowing the temperature along the wire to be considered effectively uniform.

CONCLUSION

We conducted XEOL analysis using an 80 nm-diameter x-ray nanobeam on β-Ga_2O_3:Cr NW containing optical microcavities fabricated by drilling DBR structures. Sharp resonances were observed in both NUV-B and R-NIR spectral regions. While the majority of the peaks in the R-NIR band were attributed to axial FP resonances, the resonance positions in the NUV-B band did not conform to this model. Instead, these features were well explained by WGMs along the wire's cross section. The XEOL spectra demonstrated a clear dependence on the x-ray photon flux. The intensity ratio between the NUV-B and R-NIR bands varied significantly: the NUV-B band was nearly quenched at lower fluxes (~10^9 photons per second, 10.52 keV photon energy) but became comparable in intensity to the R-NIR band at higher fluxes (~10^{11} photons per second, 10.52 keV photon energy). X-ray-induced local heating caused notable redshifts in the FP peaks within the R-NIR band, enabling the determination of the cavity's local temperature operating in two different beam modes. In addition, WGM peaks in the β-Ga_2O_3 NUV-B band also exhibited redshifts attributed to irradiation-induced heating. Both experimental analysis and FDTD COMSOL simulations confirmed this irradiation-induced local heating, revealing a local temperature increase from room temperature up to 356 K for the range of analyzed x-ray photon fluxes. The COMSOL simulations further corroborated the general conclusions obtained from the experimental results, showing a uniform temperature along the NW.

ACKNOWLEDGMENTS

The authors thank the ESRF for granting beamtime for this work on beamline ID16B (experiment MA-5727) and extend their gratitude to Valentina Bonino for her support as local contact during the experiment. This work was supported by MCIN Project No. PID2021-122562NB-I00, Grant No. TED2021-130139BI00, and Grant No. PDC2023-145868-I00; funded by Grant No. MCIN/AEI/10.13039/501100011033 and by the European Union NextGenerationEU/PRTR; Grant MAD2D-CM-UCM funded by Comunidad de Madrid, by the Recovery, Transformation, and Resilience Plan, and by Next GenerationEU from the European Union. The authors also acknowledge support from the Air Force Office of Scientific Research under Award Nos. FA8655-20-1-7013 and FA8655-23-1-7002 (Program Manager: Ali Sayir). This work made use of the FIB facilities of the SGIker of electron microscopy and microanalysis of materials from the UPV/EHU. Additional support was provided by the Deutsche Forschungsgemeinschaft (Grant No. DFG, INST 144/462-1 FUGG). M.A.-O. acknowledges the financial support from the Central Research Development Fund (CRDF) of the University of Bremen (Grant No. ZF04/2021). J.D. especially acknowledges the financial support of ESRF for his postdoctoral fellowship position.

AUTHOR DECLARATIONS

Conflict of Interest

The authors have no conflicts to disclose.

Author Contributions

D. Carrasco: Data curation (equal); Formal analysis (equal); Investigation (equal); Methodology (equal); Software (equal); Visualization (equal); Writing – review & editing (equal). **J. Dolado**: Conceptualization (equal); Data curation (equal); Formal analysis (equal); Funding acquisition (equal); Investigation (equal); Methodology (equal); Resources (equal); Validation (equal); Writing – review & editing (equal). **P. Pérez-Peinado**: Data curation (equal); Investigation (equal); Writing – review & editing (equal). **B. Rodríguez**: Investigation (equal); Methodology (equal); Software (equal); Visualization (equal); Writing – review & editing (equal). **M. Alonso-Orts**: Investigation (equal); Methodology (equal); Writing – review & editing (equal). **J. M. San Juan**: Investigation (equal); Resources (equal); Writing – review & editing (equal). **M. L. Nó**: Investigation (equal); Resources (equal); Writing – review & editing (equal). **P. Hidalgo**: Investigation (equal); Software (equal); Supervision (equal); Writing – review & editing (equal). **G. Martínez-Criado**: Funding acquisition (equal); Investigation (equal); Methodology (equal); Project administration (equal); Resources (equal); Supervision (equal); Writing – review & editing (equal). **B. Méndez**: Formal analysis (equal); Funding acquisition (equal); Investigation (equal); Methodology (equal); Project administration (equal); Writing – review & editing (equal). **E. Nogales**: Conceptualization (equal); Formal analysis (equal); Funding acquisition (equal); Investigation (equal); Methodology (equal); Project administration (equal); Supervision (equal); Validation (equal); Visualization (equal); Writing – original draft (equal); Writing – review & editing (equal).

DATA AVAILABILITY

The data that support the findings of this study are available from the corresponding author upon reasonable request.

REFERENCES

[1] M. Higashiwaki, K. Sasaki, A. Kuramata, T. Masui, and S. Yamakoshi, Appl. Phys. Lett. **100**, 013504 (2012).
[2] J. A. Spencer, A. L. Mock, A. G. Jacobs, M. Schubert, Y. Zhang, and M. J. Tadjer, Appl. Phys. Rev. **9**, 011315 (2022).
[3] S. J. Pearton, J. Yang, P. H. Cary, F. Ren, J. Kim, M. J. Tadjer, and M. A. Mastro, Appl. Phys. Rev. **5**, 011301 (2018).
[4] A. Bednarkiewicz, L. Marciniak, L. D. Carlos, and D. Jaque, Nanoscale **12**, 14405 (2020).
[5] N. W. Gong, M. Y. Lu, C. Y. Wang, Y. Chen, and L. J. Chen, Appl. Phys. Lett. **92**, 073101 (2008).
[6] V. Mykhaylyk, H. Kraus, Y. Zhydachevskyy, V. Tsiumra, A. Luchechko, A. Wagner, and A. Suchocki, Sensors **20**, 5259 (2020).

[7]M. Alonso-Orts, E. Nogales, J. M. San Juan, M. L. Nó, J. Piqueras, and B. Méndez, Phys. Rev. Appl. **9**, 064004 (2018).
[8]M. Alonso-Orts, G. Chilla, R. Hotzel, E. Nogales, J. M. San Juan, M. L. No, M. Eickhoff, and B. Mendez, Optics Letters **46**, 278 (2021).
[9]M. Alonso-Orts, R. J. T. Neelissen, D. Carrasco, M. Schowalter, A. Rosenauer, E. Nogales, B. Méndez, and M. Eickhoff, Adv. Mater. Technol. **10**, 2400881 (2025).
[10]M. Alonso-Orts, D. Carrasco, J. M. San Juan, M. L. Nó, A. de Andrés, E. Nogales, and B. Méndez, Small **18**, 2105355 (2022).
[11]D. Carrasco, E. Nieto-Pinero, M. Alonso-Orts, R. Serna, J. M. San Juan, M. L. Nó, J. Jesenovec, J. S. McCloy, E. Nogales, and B. Méndez, Nanomaterials **13**, 1126 (2023).
[12]L. M. Barmore, J. Jesenovec, J. S. McCloy, and M. D. McCluskey, J. Appl. Phys. **133**, 175703 (2023).
[13]E. L. Bright, C. Giacobbea, and J. P. Wright, J. Synchrotron Radiat. **28**, 1377 (2021).
[14]V. Bonino, D. Torsello, C. Prestipino, L. Mino, and M. Truccato, J. Synchrotron Radiat. **27**, 1662 (2020).
[15]G. Martínez-Criado, J. Villanova, R. Tucoulou, D. Salomon, J.-P. Suuronen, S. Labouré, C. Guilloud, V. Valls, R. Barrett, E. Gagliardini, Y. Dabin, R. Baker, S. Bohic, C. Cohen, and J. Morse, J. Synchrotron Radiat. **23**, 344–352 (2016).
[16]E. Nogales, J. A. García, B. Méndez, and J. Piqueras, J. Appl. Phys. **101**, 033517 (2007).
[17]Y. K. Frodason, K. M. Johansen, L. Vines, and J. B. Varley, J. Appl. Phys. **127**, 075701 (2020).
[18]I. Bhaumik, R. Bhatt, S. Ganesamoorthy, A. Saxena, A. K. Karnal, P. K. Gupta, A. K. Sinha, and S. K. Deb, "Temperature-dependent index of refraction of monoclinic Ga_2O_3 single crystal," Appl. Opt. **50**, 6006 (2011).
[19]M. Alonso-Orts, E. Nogales, J. M. San Juan, M. L. No, and B. Mendez, Proc. SPIE **10919**, 109191S (2019).
[20]H. Oda, N. Kimura, D. Yasukawa, H. Wakai, and A. Yamanaka, Physica Status Solidi A **214**, 1600670 (2017).
[21]Y. Tokida and S. Adachi, J. Appl. Phys. **112**, 63522 (2012).
[22]V. A. Solé, E. Papillon, M. Cotte, P. Walter, and J. Susini, "A multiplatform code for the analysis of energy-dispersive x-ray fluorescence spectra," Spectrochim. Acta, Part A **62**, 63–68 (2007).
[23]Z. Guo, A. Verma, X. Wu, F. Sun, A. Hickman, T. Masui, A. Kuramata *et al.*, Appl. Phys. Lett. **106**, 111909 (2015).
[24]D. Wu, N. Xia, K. Ma, J. Wang, C. Li, Z. Jin, H. Zhang, and D. Yang, Crystals **12**, 1715 (2022).